Acta Acustica 2024, **8**, 38
© The Author(s), Published by EDP Sciences, 2024
https://doi.org/10.1051/aacus/2024015

Available online at:
https://acta-acustica.edpsciences.org

SCIENTIFIC ARTICLE OPEN ACCESS

Uncoupled multimodal wave reflection from guide termination with different flanges: Experimental and numerical investigation

David Marx*, Florent Margnat, Hélène Bailliet, Christian Prax, Zhiping Qiu, and Jean-Christophe Valière

Institut Pprime, CNRS – Université de Poitiers – ISAE-ENSMA, ENSIP, Bâtiment B17, 6 Rue Marcel Doré, TSA 41105, 86073 Poitiers Cedex 9, France

Received 27 October 2023, Accepted 5 May 2024

Abstract – Reflection of propagating modes is studied at the exit of a cylindrical acoustic wave guide from both an experimental and a numerical point of view. The plane mode and several purely azimuthal higher modes are extracted by means of modal decomposition and the uncoupled reflection coefficients of each mode are obtained using two microphonic antennas for Helmholtz numbers below 5.3. The reflection at the open end of the guide is studied for different guide terminations: without flange, with a finite flange, with an infinite rigid flange. A numerical model based on finite elements is set to mimic the experimental protocol: generation of the acoustic wave by a locally vibrating wall (to represent the flush-mounted loudspeakers used in the experiments), computation of the acoustic field in a cylindrical duct geometry and radiation in open space (represented by a half sphere). Results are also compared with the theoretical predictions from the literature when available. For the plane mode, the difference between the three sources of data is less than 5%; overall, the agreement allows to discern an effect of termination for the plane mode and for the first higher mode. An end with finite flange leads to intermediate behaviours between without flange and with an infinite flange only for the reflection coefficient of the plane mode.

Keywords: Reflection of acoustic waves, Duct acoustics, Microphone antenna, Multimodal propagation, End correction

1 Introduction

Although it is a classical problem of acoustics, prediction and measurement of sound reflection at the exit of an open guide is not straightforward. The problem depends on the frequency range and the cross dimensions of the duct. At low frequencies, for which the wavelengths are large compared to the duct radius, only the plane wave propagates. Many studies of sound radiation from a wave guide have been concerned with this plane wave regime. Various detailed calculations of the reflection of the plane wave at the open end of a guide for unflanged [1] and infinitely flanged [2–4] are available. Ando also provided a solution for the reflection of the plane wave at the open end of a circular duct including thick walls [3]. In addition, experimental investigations for various flanges have been compared to theoretical and numerical results [5]. The case of sound radiation with a mean flow has also received great attention due to its importance for the understanding of noise generated by aircraft jet engine or air conditioning systems (e.g. [6]).

At high frequencies, high-order modes can propagate in addition to the plane wave, which increases the complexity of the sound field. These modes appear as the frequency exceeds their respective cut-on frequencies. The description of reflection back into the guide, scattering into other modes and radiation outside the guide are more complicated than in the plane wave regime. Whatever the mode, its reflection depends on the geometry of the duct termination. The literature on radiation of higher modes is less developed and more theoretically or numerically oriented than the one for plane waves. Zorumski [7] derived an equation for the multimodal reflection matrix in the case of an infinitely flanged guide. Rienstra [8] proposed an analytical description of reflection and conversion coefficients of higher modes in circular and annular unflanged duct including the effect of a mean flow. Snakowska et al. [9, 10] presented a numerical approach of multimodal radiation for the same geometry, including reflection coefficient together with length correction calculations. Dahl et al. [11] compared reflection coefficients obtained from in-guide measurements with those determined from numerical code calculation for an unflanged duct. The results did not agree and a subsequent study was proposed to determine the accuracy of computed results for unflanged, flanged and thin guides [12].

---

*Corresponding author: david.marx@univ-poitiers.fr

Multimodal radiation impedance can also be computed numerically for circular ducts of arbitrary wall thickness [13] or for an arbitrary cross-sectional shape in an infinite baffle [14].

On the experimental side, studies of acoustic modes separation in cylindrical guides were published from the seventies [15, 16]. Kerschen and Johnston [17] proposed a measurement technique which performs modal separation of broadband noise propagating in circular ducts. They used $2n$ microphones, spaced around the circumference of the duct, to extract the $(n-1)$ order of circumferential modes instantaneously. Åbom [18] used an extension of the two-microphone transfer function method [19] which allowed for the first time to get not only the mode decomposition but also several terms of the reflection and transmission matrices. Akoum and Ville [20] proposed a technique of measuring the reflection matrix for duct discontinuities with higher-order modes based on the measurement of the acoustic pressure by microphone pairs in two cross sections and separation of incident and reflected modes by use of Fourier-Lommel transform. In the context of analysis of noise generated by orifice plate in ducts, Horner and Hu [21] developed a hybrid modal decomposition approach to deconstruct the in-duct sound field into individual higher-order mode contribution. In their approach, the process of modelling the sound field is simplified by using uncoupled calculations for the higher order modes. Uncoupled here refers to the fact that a reflected mode of some order is mainly generated by the incident mode of the same order, cross-couplings between modes of different orders remaining negligible. In [21] this is associated with a limited number of measurements locations in the duct therefore with a rapid decomposition. Further results by the same authors [22] showed that the proposed hybrid decomposition approach was efficient in estimating the propagation in a duct with several orifices. Other beamforming-inspired deconvolution methods, such as DAMAS, can be used to retrieve modal amplitudes from flush-mounted microphones, including their correlations [23].

The objective of the present work is to carry out a sufficiently precise modal decomposition in order to distinguish the reflection coefficients of different terminations for the first higher-order modes in a cylindrical waveguide. We will restrict ourselves to the measurement of the reflection coefficients in a mid-frequency range so that the uncoupled approach as defined above is justified. This permits a great simplification of the description of the multi-mode wave propagation and also reduces the number of microphones to be used in the experimental study. This mid-frequency range extends to Helmholtz numbers up to 5 approximately. In this range, the only modal conversion at the duct termination is between the plane mode and the first radial mode having no azimuthal dependence [20]. A consequence of this is that, at sufficient distance from the termination, uncoupling is indeed valid for the first three azimuthal modes in the mid-frequency range, and for the plane mode in a low-end sub-range of the latter, with a limit to be specified below. This still allows to study reflection for different terminations and provides simple experimental and numerical tools useful for practical engineering applications. A test bench has been developed to study multimodal acoustic reflection at different duct terminations without any mean flow. The reflection coefficients and end corrections are extracted using the classical two microphones method [19, 24] but replacing the two microphones by two microphone rings of 8 microphones each. For the plane wave, results are compared with the models from the literature: without flange given by Levine and Schwinger [1], with a finite flange given by Dalmont et al. [5] and with an infinite rigid flange given by Norris and Sheng [4]. For higher order modes, references exist without flange [8, 10] and with infinite flange [7], but since no model is available for an arbitrary termination, a numerical model of the experiment is used for comparisons. The paper is organized as follows. In Section 2 the experimental setup, the principle of measurements and the estimation of the modes are presented. The same model is used for the modal decomposition in the experimental and in the numerical approach, which is presented in Section 3. Results for reflection coefficients and end corrections are presented for the different terminations in Section 4.

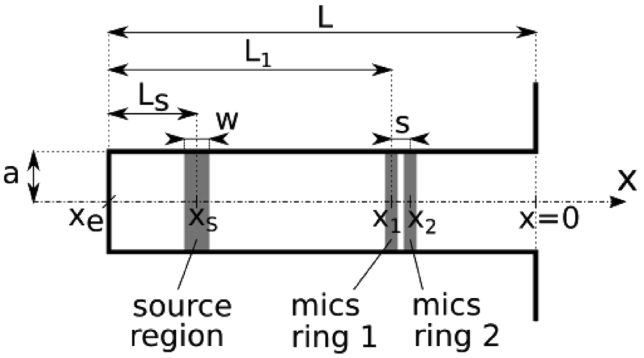

Figure 1. Schematic of the duct (not to scale). $L = 1.32$–1.39 m (depending on termination); $a = 0.088$ m; $L_1 = 1.21$ m; $L_s = 0.54$ m; $s = x_2 - x_1 = 0.04$ m; $w = 0.09$ m; microphones are 1/4". Not to scale.

2 Experimental setup and propagation model

2.1 Guide, source and microphone arrays

We consider a circular wave guide made of rigid walls, as shown schematically in Figure 1. The inner radius of the duct is $a = 0.088$ m, corresponding to a 1143 Hz cut-on frequency for the first higher mode. One extremity is closed, the other is open and sound radiates in an anechoic room, the source region standing at the entrance of the anechoic room. At the duct open end, three different terminations can be used, as shown in Figure 2. These are: a very thin-edges termination (unflanged case), a termination with an infinite flange, and a termination having a finite flange, which is an intermediate situation between the former two. The length $L = -x_e$ of the duct depends slightly on which termination is used and varies between 1.32 m and 1.39 m. The thickness of the infinite flange is 22 mm.

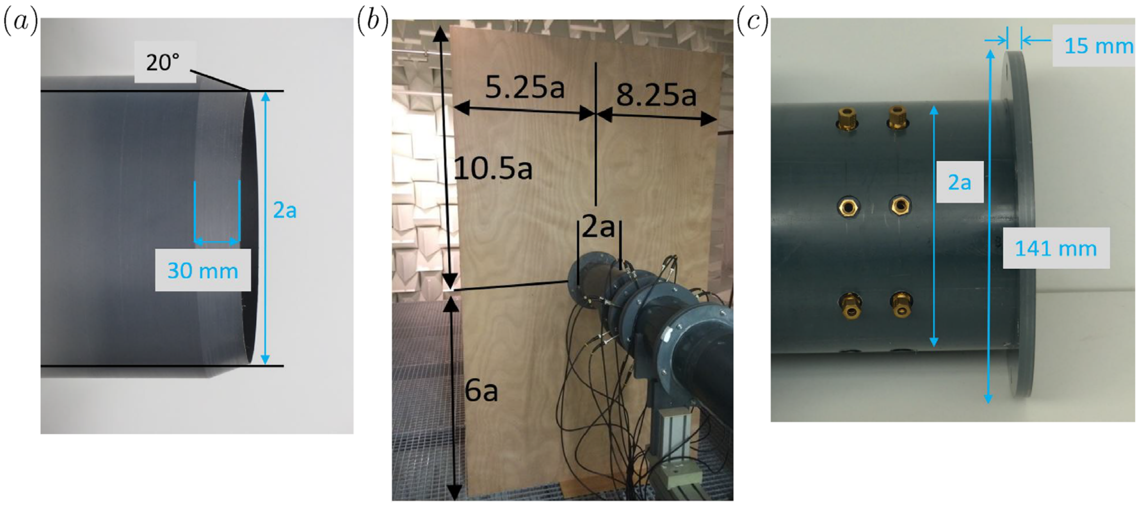

Figure 2. Terminations: (a) unflanged, (b) infinite flange, (c) finite flange.

The wave guide is excited by an acoustic source, described in [26], composed of 16 loudspeakers (Morel MDM55 having a flat response for a wide frequency range, with −3 dB cut-off frequencies at 450 Hz and 8500 Hz.). The center of this source is located at a distance $L_s = x_s - x_e = 0.54$ m from the rigid end of the duct, and its width is about $w = 0.33$ m. The source is excited by a sinusoidal signal and frequency is swept from 50 Hz to 3300 Hz in 5 Hz increments. The duration of excitation is 30 s for each working frequency and the chosen frequency range allows to cover 5 propagating modes. For the present study, only one pair of diametrically opposed loudspeakers is used and the relative phase between them is adjusted to favor the excitation of each given mode. An azimuthal mode will be preferably excited if the loudspeakers generate signals whose phase follow that associated with the target mode. For example, the two loudspeakers diametrically opposed have to be set out of phase to favor the (1, 0) mode and the (3, 0) mode, or in phase to favor the (0, 0) mode, where the mode orders $(m,\ n)$ are defined in the next section. Using such phase relationship yields significant improvement of signal to noise ratio for frequencies above the first cut-on frequency [33].

The pressure in the duct is measured using a microphone antenna. Figure 3 shows the antenna consisting of 2 rings of M microphones each, with $M = 8$. On a given ring, the microphones are equidistant, separated by a $\frac{2\pi}{M} = \frac{\pi}{4}$ angle. The first ring is at a distance $L_1 = x_1 - x_e =$ 1.21 m from the rigid end, and the distance between the two rings is $s = x_2 - x_1 = 0.04$ m. The class 1 microphones (BSWA TECH type MPA451, frequency response 10 Hz to 50 kHz) are plugged to the guide via an orifice smaller than the diameter of the microphone. The diameter of the orifice is 6.8 mm and its length is 0.8 mm therefore the resonance frequency of the very small plug-in cavity in front of the microphone is much higher than the frequencies of interest in this study. The acquisition is performed by an ETEP Universal Recorder System 8.5.1. that has a 100 kHz sampling frequency [33]. The synchronous detection method is used to extract the microphone pressure recorded for 30 s for each frequency step. A thermocouple measurement allows to adjust the speed of sound to the actual ambient conditions.

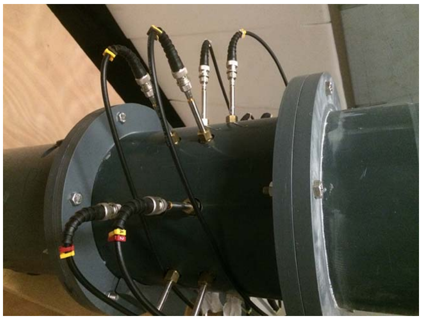

Figure 3. Microphone antennas.

2.2 Propagation model

In this section, we present the classical multimodal sound propagation in a circular duct. It is intended to describe sound propagation in the rigid section downstream of the source, between $x = x_s$ and $x = 0$. Then, the open end of the duct at $x = 0$ is considered and the reflection coefficient at this extremity is introduced. The implication of the choice of a rigid reflecting termination at the other end of the duct at $x = x_e$ is finally briefly discussed.

Cylindrical coordinates are denoted by x, r, θ. The propagation of sound within the guide in the section located between $x = x_s$ and $x = x_e$ is governed by the following wave equation and boundary conditions:

$$\begin{cases} \dfrac{\partial^2}{\partial t^2}p - c_0^2\left(\dfrac{\partial^2}{\partial r^2}+\dfrac{1}{r}\dfrac{\partial}{\partial r}+\dfrac{1}{r^2}\dfrac{\partial^2}{\partial \theta^2}+\dfrac{\partial^2}{\partial x^2}\right)p = 0 \\ \left.\dfrac{\partial p}{\partial r}\right|_{r=a} = 0 \quad \text{(rigid wall)} \end{cases} \tag{1}$$

where c_0 is the sound speed. The acoustic pressure within the lossless guide can be expressed as a combination of eigenmodes according to [27]:

$$p(x,r,\theta,t) = \int_{-\infty}^{\infty} \sum_{m=-\infty}^{\infty} \sum_{n=0}^{\infty} J_m\left(\kappa_{mn}\frac{r}{a}\right)[A^+_{mn}e^{-j\gamma_{mn}x} + A^-_{mn}e^{j\gamma_{mn}x}]e^{-jm\theta}e^{j\omega t}\,\frac{\mathrm{d}\omega}{2\pi}, \tag{2}$$

where ω is the angular frequency, with corresponding wavenumber in free space $k = \omega/c_0$. Equation (2) states that the pressure field is the sum of modes indexed by integers (m, n) where $m = -\infty...\infty$ is the azimuthal order, and $n = 0,...,\infty$ is the radial order. Each mode contains a right-propagating component of amplitude $A^+_{mn}(\omega)$ and a left-propagating component of amplitude $A^-_{mn}(\omega)$. The radial shape of the modes is determined by J_m which is the mth Bessel function of the first kind, and denoting by k_{mn} the $(n+1)$th zero of its derivative gives $J'_m(\kappa_{mn}) = 0$ (note that in the present notations $n = 0$ corresponds to the first zero). Each mode is associated with an axial wavenumber $\gamma_{mn} = \sqrt{k^2 - (\frac{\kappa_{mn}}{a})^2}$, which is real if the mode propagates and imaginary if it is cut-off. A given mode is propagating (resp, cut-off) if ω is larger (resp, lower) than its cut-off angular frequency defined by $\omega_{c,mn} = \frac{c_0\kappa_{mn}}{a}$; equivalently, the cut-off frequency is $f_{c,mn} = \frac{c_0\kappa_{mn}}{2\pi a}$. The values of κ_{mn} and $f_{c,mn}$ for the first cut-on modes (m, n) are given in Table 1. In this table, $a = 0.088$ m and $c_0 = 343.2$ m·s^{-1} are used, which corresponds to our experimental apparatus. For frequencies up to 3300 Hz, under study in this paper, only the modes listed in this table are propagating. This corresponds to the following range for the Helmholtz number: $ka = \omega a/c_0 < 5.3$.

We now consider the open end of the duct, at $x = 0$, and introduce the reflection coefficient, which is the quantity of interest in this work both experimentally and numerically. At the open end of the guide, a given propagating mode is partly radiated outward, and partly reflected back into the duct, where it is transformed into other modes of the same circumferential order but of arbitrary radial order. As a result, the amplitude of a mode travelling from the duct open extremity is [7]:

$$A^-_{mn} = \sum_{q=0}^{\infty} R_{mnq}A^+_{mq}, \tag{3}$$

where R_{mnq} can be seen as the components of a reflection matrix. Note that we have fixed $x = 0$ at the open end (as in [7]), otherwise extra phase factors would be present in equation (3). In general the reflection of a mode onto itself is prevailing, that is, $R_{mnn} \gg R_{mnq}$ for $q \neq n$, yielding $R_{mnn} \sim A^-_{mn}/A^+_{mn}$. This relation, which consists in supposing that the modes are uncoupled, is only an approximation, but it may become exact in certain frequency ranges that we are going to consider. In particular, for the mode (0, 0), the expansion reads: $A^-_{00} = R_{000}A^+_{00} + R_{001}A^+_{01} + R_{002}A^+_{02} + ...$ In the present work, the frequency range ($f <$ 3300 Hz) limits the number of propagating modes, meaning $A^+_{0q} = 0,\ \forall q \leq 2$, provided measurements are performed sufficiently far from discontinuities or sources. Below the cut-on frequency of mode (0,1), we also have $A^+_{01} = 0$. However, for $f > f_{c,01}$ we have $A^+_{01} \neq 0$ and $A^-_{00} = R_{000}A^+_{00} + R_{001}A^+_{01}$, meaning $R_{000} \neq A^-_{00}/A^+_{00}$. Similar analysis for the other azimuthal mode orders gives the following expression for the reflection coefficients to be extracted from the experiments:

Table 1. List of all propagating modes (m, n) in the frequency range under study (1st column), with associated value of κ_{mn} (2nd column) and cut-off frequency (3rd column).

Mode (m, n)	κ_{mn}	$f_{c,mn}$ (Hz)
(0, 0)	0	0
(1, 0)	1.8412	1143
(2, 0)	3.0542	1896
(0, 1)	3.8317	2379
(3, 0)	4.2012	2608

$$R_{000} = A^-_{00}/A^+_{00} \qquad f < f_{c,01}, \tag{4}$$

$$R_{100} = A^-_{10}/A^+_{10}\ red \qquad f_{c,10} < f < f_{c,11}, \tag{5}$$

$$R_{200} = A^-_{20}/A^+_{20} \qquad f_{c,20} < f < 3300\,\text{Hz}, \tag{6}$$

$$R_{300} = A^-_{30}/A^+_{30} \qquad f_{c,30} < f < 3300\,\text{Hz}\,. \tag{7}$$

Results for R_{000} will therefore be presented only for frequencies below the cut-on frequency of mode (0, 1), and those for R_{100} below the cut-on frequency of mode (1, 1). Equations (4)–(7) are correct as long as measurements are performed far from any discontinuity or source. Also, note that we have not used any transverse mode normalization in equation (2). In general, the reflection coefficient depends on the particular normalization used, but this is not the case for R_{m00} considered here (since any normalization would multiply both A^+_{m0} and A^-_{m0} by the same factor).

The termination at $x = x_e$ in this work is taken to be rigid and the consequence of this is discussed. First, it should be noted that the reflection coefficient at the open end of the duct is fixed by the open-end termination at $x = 0$ only. In particular, it does not depend on the nature of the termination at the other end. At least this is true as long as this other end is not open itself, which would create a coupling between the two extremities through the outside of the duct [29]. However, the use of a rigid termination at $x = x_e$ has an impact on the global sound field within the duct and this may have practical consequences. In particular this creates resonances and anti-resonances in the duct (see also the discussion of Fig. 6). If microphone antennas are located close to a pressure node, finding the mode amplitudes from the microphone signals (which is the inverse problem presented in the next section) is badly conditioned. In the present experimental setup this has been avoided by using, among several initially possible loudspeaker axial locations, the one for which this problem does not occur. Another option would have been to use an absorbing termination made of foam, or to use more antennas with uneven spacing between them.

2.3 Inverse problem

In order to obtain the reflection coefficients R_{m00} by using equations (4)–(7), it is necessary to compute $A^{\pm}_{m0}$ from the measured microphone signals at the antenna. This inverse problem is solved by using a multimodal extension of the two-microphone technique. In each antenna, the M microphones are located at equispaced angles θ_q, with $q = 0, \ldots, M{-}1$, and at the wall ($r = a$). Taking the Fourier transform in time of equation (2) written at $r = a$ and $\theta = \theta_q$, gives the pressure p_q for microphone at angle θ_q:

$$p_q(x,\omega) = \sum_{m=-\infty}^{\infty} P_m(x,\omega) e^{-j2\pi mq/M}$$

$$= \sum_{m=-M/2}^{M/2-1} P_m(x,\omega) e^{-j2\pi mq/M} \qquad (\forall q = 0, \ldots, M-1), \quad (8)$$

where the second equality is due to the fact that a limited number of azimuthal modes can be measured using the antenna, which is valid in the frequency range of interest, and where

$$P_m(x,\omega) = \sum_{n=0}^{\infty} J_m(\kappa_{mn})[A^+_{mn}e^{-j\gamma_{mn}x} + A^-_{mn}e^{j\gamma_{mn}x}] \quad (9)$$

$$= J_0(\kappa_{m0})[A^+_{m0}e^{-j\gamma_{m0}x} + A^-_{m0}e^{j\gamma_{m0}x}] \quad \left(\forall m = -\frac{M}{2}, \ldots, \frac{M}{2} - 1\right). \quad (10)$$

The transition from equations (9) and (10) is possible when only the modes of radial order $n = 0$ are present, which is the case in the whole frequency range for $|m| = 2, 3$, in the range $f < f_{c,01}$ for $m = 0$, and in the range $f < f_{c,11}$ for $|m| = 1$, in line with the frequency range in which equations (4)–(7) are valid. The second sum in equation (8) is a discrete Fourier transform. The amplitudes P_m are then obtained from the inverse discrete Fourier transform

$$P_m(x,\omega) = \frac{1}{M}\sum_{q=0}^{M-1} p_q(x,\omega) e^{j2\pi mq/M}. \quad (11)$$

Pressure measurements are performed at the two rings located at $x = x_1$ and $x = x_2$, therefore giving access to $p_q(x_1, \omega)$ and $p_q(x_2, \omega)$, and in turn to $P_m(x_1, \omega)$ and $P_m(x_2, \omega)$ from equation (11). Writing equation (10) at the two positions gives:

$$J_0(\kappa_{m0})[A^+_{m0}e^{-j\gamma_{m0}x_1} + A^-_{m0}e^{j\gamma_{m0}x_1}] = P_m(x_1,\omega) \quad (12)$$

$$J_0(\kappa_{m0})[A^+_{m0}e^{-j\gamma_{m0}x_2} + A^-_{m0}e^{j\gamma_{m0}x_2}] = P_m(x_2,\omega) \quad (13)$$

so that the reflection coefficient at the end of guide can be expressed as

$$R_{m00}(\omega) = \frac{A^-_{m0}}{A^+_{m0}} = \frac{P_m(x_2,\omega) - P_m(x_1,\omega)e^{-j\gamma_{m0}(x_2-x_1)}}{P_m(x_1,\omega)e^{j\gamma_{m0}(x_2-x_1)} - P_m(x_2,\omega)} e^{-2j\gamma_{m0}x_1}. \quad (14)$$

This is the main outcome of the microphone antenna processing in the experiments or simulations and will be discussed below. The expression is valid for frequencies below $f_{c,01}$ for R_{000}, below $f_{c,11}$ for R_{100}, and below 3300 Hz for R_{200} and for R_{300}. R_{m00} is a complex quantity, and it is customary to represent its modulus, $|R_{m00}(\omega)|$, and, rather than its phase, its end correction, $\delta_{m00}(\omega)$. This characterizes the inertial character of the open termination of the guide and is defined implicitely as $R_{m00}(\omega) = -|R_{m00}(\omega)|e^{-2j\gamma_{m0}(\omega)\delta_{m00}(\omega)}$. This is an extension to the multimodal case of the expression usually given for the plane wave [1, 28]. This extension is particularly justified for the reflection coefficient R_{m00} since this has a value close to -1 at the cut-on frequency of mode $(m, 0)$, just as the plane mode at zero frequency. An explicit expression is:

$$\delta_{m00}(\omega) = \frac{j}{2\gamma_{m0}(\omega)} \ln\left(\frac{-R_{m00}(\omega)}{|R_{m00}(\omega)|}\right). \quad (15)$$

Such an extension to higher order modes was also proposed in [10]. Equations (14) and (15) were obtained under the assumption that the non-propagating modes have a null amplitude at the microphone rings. They will be used in the following to compute R_{m00} from the experiments or numerical simulations.

2.4 Estimation of modes, calibration and data adjustment

Equation (14) makes it apparent that the correctness of the calculated reflection coefficient depends critically on the accurate calibration of the microphones, with respect to both their amplitude and their phase. Calibration of microphones is usually achieved using a piston-phone; this consists in placing each microphone in a sound field with a known pressure level at a single given frequency. When phase calibration is needed, each microphone response is generally compared to the response given by a reference microphone under the same broadband sound field. This allows to obtain the relative phase response as a function of frequency between the two microphones.

These usual calibration methods however does not account for slight changes, a couple of percents of the pressure amplitude, in the microphone response in situ compared to its non-mounted response. These slight changes, that were observed in our set up thanks to preliminary experiments, are due to minute variations in the ambient conditions and in the position of the microphone in its housing when mounted. To cope with this problem, several techniques of in-situ calibration have been developed in other contexts [30, 31]. In the present study, because we aim to achieve the required precision to faithfully reveal the difference of higher modes reflection coefficients and length corrections for different terminations, a two-step calibration was performed: first the sensitivity of each microphone was determined using a piston-phone; then the calibration was adjusted once the microphones were mounted, for both amplitude and phase. Using the above presented modal structure of the acoustic field is the basis of the adjustment: for each frequency range between cut-off frequencies, the number and structure of propagating modes are known; this yields an a priori for the pressure distribution along the circumference at each microphone ring. In the following, the method is presented when applied to two frequency ranges: below the (1, 0) cut-off frequency and between (1, 0) and (2, 0) cut-on frequencies. The same principle is applied for other frequency ranges.

Adjusting the microphone responses relies on equations (8) and (11). Based on existing calibration, the measured microphone pressures $p_q(x_1, \omega)$ yield a first estimation (indicated by a hat) of the modal amplitudes that writes, in the case of the first ring:

$$\hat{P}_m(x_1, \omega) = \frac{1}{M} \sum_{q=0}^{M-1} p_q(x_1, \omega) e^{j2\pi mq/M}. \tag{16}$$

Below the first cut-on frequency, $f_{c,10}$, and far from any discontinuity, only the plane mode should be present, meaning that we should have:

$$\hat{P}_m(x_1, \omega) = \hat{P}_0(x_1, \omega)\delta_{m,0} \tag{17}$$

that is, only $\hat{P}_0$ should be non zero. In this equation, $\delta_{m,0}$ is the Kronecker delta function. However, this is not exactly what is observed following the mounting of the microphones. In the application of equation (11), the pressure at microphone q is adjusted by a factor α_q so that a modified computation of the mode amplitudes becomes:

$$P_m(x_1, \omega) = \frac{1}{M} \sum_{q=0}^{M-1} \alpha_q(\omega) p_q(x_1, \omega) e^{j2\pi mq/M} \quad (\forall m = 0, \ldots, M-1). \tag{18}$$

The values of $\alpha_q(\omega)$ are determined by imposing that only the plane mode is detected according to:

$$\begin{aligned} P_m(x_1, \omega) &= \frac{1}{M} \sum_{q=0}^{M-1} \alpha_q(\omega) p_q(x_1, \omega) e^{j2\pi mq/M} \\ &= \hat{P}_0(x_1, \omega)\delta_{m,0} \; (\forall m = 0, \ldots, M-1) \end{aligned} \tag{19}$$

where the plane wave amplitude is forced to be the initially estimated one, $\hat{P}_0$. The effect of this adjustment is to enforce the rejection of modes which should not be present. For each frequency, the former equation is a system for the coefficients $\alpha_q(\omega)$, which is solved analytically. The computed values $\alpha_q(\omega)$ are then used all along the measurement in the range from 0 Hz to the first cut-on frequency. Figure 4 shows the result of this plane mode calibration for the first antenna used in this study. The set of coefficients $\alpha_q(\omega)$, that quantify the change due to the adjusted calibration, have a mean value that is between 0.98 and 1.01 depending on the microphone for frequencies up to approximately 1070 Hz and it goes from 0.8 to 1.1 when the frequency gets close to the first cut-on frequency.

The adjustment of calibration coefficients when higher modes are present consists in extending the previous method beyond the first cut-on frequency. For the working frequencies between the first and the second cut-on frequency, the plane mode but also the modes (±1, 0) propagate. As previously, the initial calibration is used to compute a first estimation of the modal amplitudes, $\hat{P}_m$. Then, microphone response adjustment factors $\alpha_q(\omega)$ are searched by imposing that the new estimation of the amplitudes should be zero for non propagating modes:

$$\begin{aligned} P_m(x_1, \omega) &= \frac{1}{M} \sum_{q=0}^{M-1} \alpha_q(\omega) p_q(x_1, \omega) e^{j2\pi mq/M} \\ &= \hat{P}_0\delta_{m,0} + \hat{P}_1\delta_{m,1} + \hat{P}_{-1}\delta_{m,-1} \quad (\forall m = 0, \ldots, M-1). \end{aligned} \tag{20}$$

For each frequency, this a linear system to solve to obtain the values of $\alpha_q(\omega)$. These factors are used to correct microphone amplitudes between the first and second cut-on frequencies. The process can be repeated in the other frequency ranges, and for the second microphone ring. The adjustment of calibration was performed for modes (0, 0), (1, 0), (2, 0), (3, 0). Away from cut-on frequencies, for the first antenna, $\alpha_q(\omega)$ for the different modes are between 0.99 and 1.01 for mode (1, 0), between 0.97 and 1.04 for mode (2, 0), and between 0.89 and 1.12 for mode (3, 0), showing a slight increase of the correction with the frequency. The adjustment for the second antenna yields corrections for each mode that are close to these values.

2.5 Example of modal decomposition result

Figure 5 shows an example of results for the pressure amplitude obtained for the different modes extracted by the 8 microphones of the first ring. As expected, the plane mode amplitude (blue) is high for all the working frequencies. At the first cut-on frequency $f_{c,10}$ the amplitude of the (1, 0) mode (green) increases greatly, as does the amplitude of higher modes ((2, 0) mode in red and (3, 0) mode in cyan) at their own cut-on frequencies. The emergence of propagating modes is very good at low frequencies (more than 40 dB for the plane mode); it decreases as the frequency increases but keeps fair for the frequency range under study. Some spikes are seen in Figure 5 and a zoom in on some of them is shown in Figure 6 which displays the pressure amplitude for the plane wave mode between 450 Hz and 700 Hz. The red vertical lines mark the frequencies of maxima of the pressure amplitude. It appears that these frequencies are related to the resonance of the whole guide, $f_{resonance} = \frac{(2n+1)c_0}{4L}$. The minima of the pressure amplitude (marked by the green lines in Figure 6) are partly associated with anti-resonances. But the values of these minima are also a complex result of interaction of the whole guide anti-resonance, the position of the microphones in the wave pattern and the efficiency of the source in exciting the guide at the given frequency. These interactions get even more complex at higher frequencies so that it is impossible to

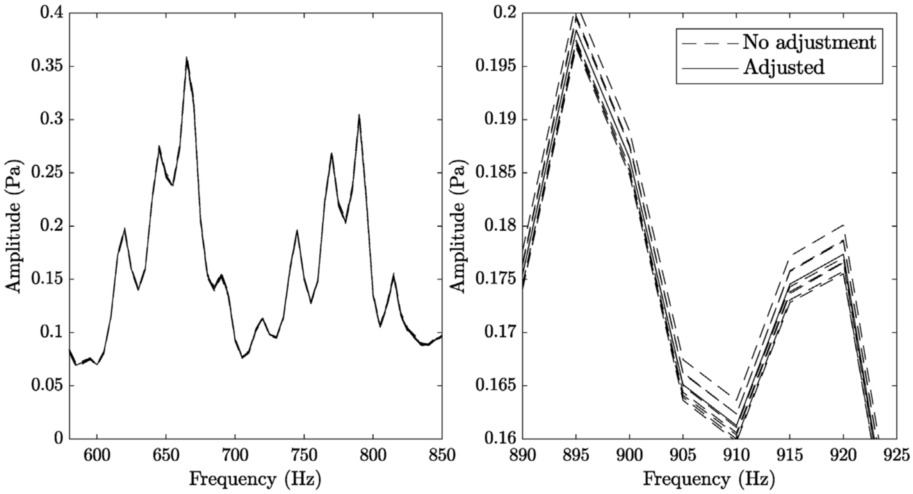

Figure 4. Adjustment of microphonic calibration for the plane mode; left: pressure amplitudes $p_q(f)$ before (dashed lines) and $p'_q(f)$ after (plain line) adjustment; right: zoom in the frequencies around 900 Hz.

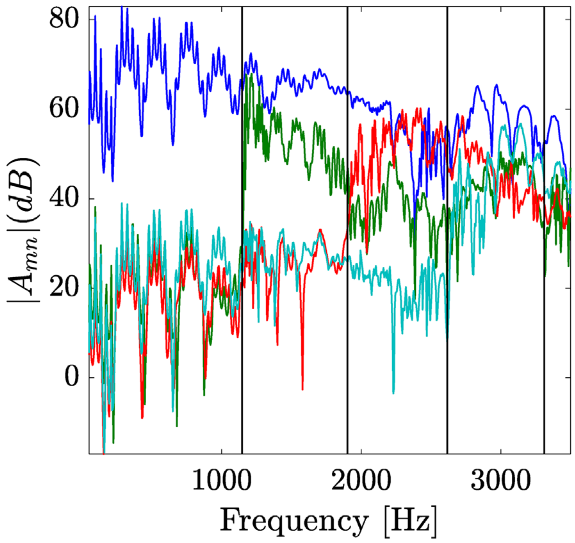

Figure 5. Modal decomposition in a guide with a termination without flange. Blue: amplitude of the plane mode; green: (1, 0) mode; red: (2, 0) mode; cyan: (3, 0) mode; the black vertical lines indicate the theoretical cut-on frequencies $f_{c,10}$, $f_{c,20}$, $f_{c,30}$.

extract any periodic pattern in Figure 5 for frequencies above $f_{c,10}$.

3 Numerical simulation of the experimental bench

Numerical simulations have been performed in order to support the experimental data, in particular for the finite flange case for which no theoretical data exist. The numerical setup is specified and validated in the present section. Simulations are carried out with the commercial, finite-element solver *Comsol Multiphysics*. Helmholtz' wave equation for pressure

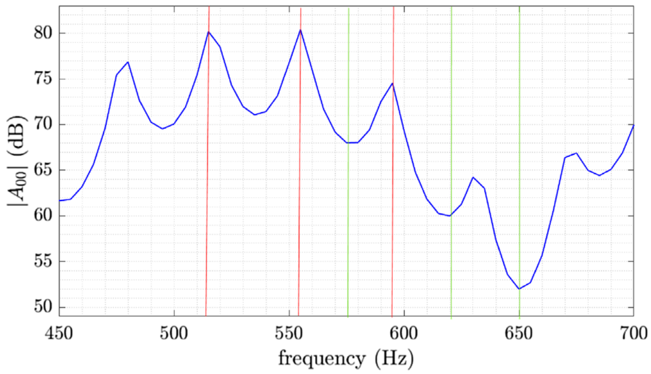

Figure 6. Pressure amplitude of plane mode (zoom in of Figure 5 between 450 Hz and 700 Hz). The red vertical lines indicate maxima of pressure amplitudes for plane mode and the green ones indicate frequencies of minima.

$$\nabla\left[\frac{1}{\rho}\nabla p\right]+\frac{k^2}{\rho}p=0 \tag{21}$$

is solved for an air medium ($c_0 = 340$ m·s^{-1} and $\rho_0 = 1.23$ kg·m^{-3}). The gradient and divergence operators are approximated with a finite element method and the resulting system is solved using the Biconjugate Gradient Stabilized algorithm. A three-dimensional model of the experimental apparatus is designed, comprising a wave guide of circular cross section having one extremity closed by a rigid plate, and the other extremity open, as sketched in Figure 7. At the outlet of the pipe, the infinite space is represented with a half sphere for a baffled pipe, while a complete sphere (nearly complete in fact, since it is limited by the duct walls) is meshed for the unbaffled and the flanged pipe. On this sphere a non-reflection boundary condition is used to faithfully simulate the radiation condition, the sphere radius R being taken sufficiently large for this to be possible. The rigid wall condition is used on the pipe

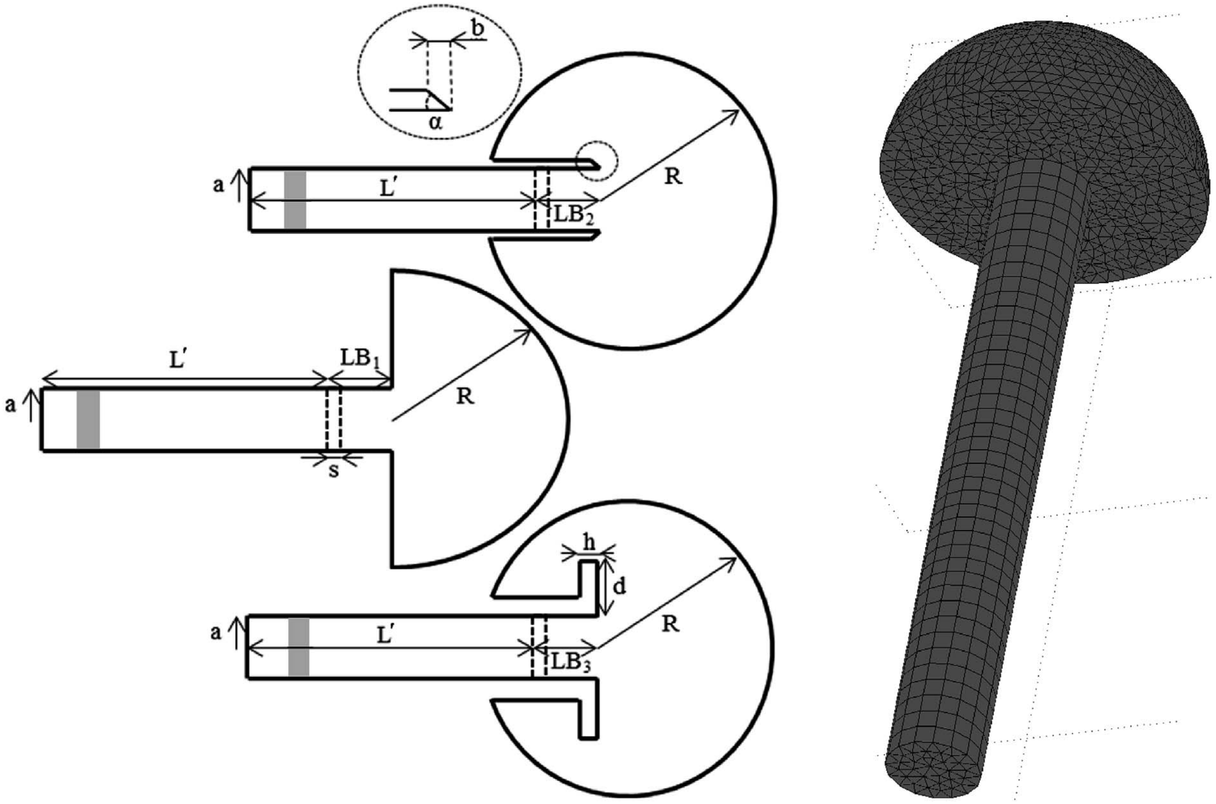

Figure 7. Simulation domain parameters for no flange, infinite flange and finite flange (left, from top to bottom, respectively; the greyed area represents the excitation location) and grid topology for infinite flange (right). On sphere portions, a non-reflecting boundary condition is specified; at excitation, an imposed acceleration is specified; all other boundaries are set as rigid walls.

walls and the baffle and the flange surfaces. In the simulations, the loudspeakers are modelled by a small vibrating portion of the pipe wall near the closed end, with imposed acceleration, with the same location L_s and width w as in the experiment (see Fig. 1). The frequency of the excitation is defined as a linear sweep with a frequency step of 10 Hz up to 3300 Hz. A typical grid is shown in Figure 7. In all of the cases, it is made of triangular prism elements in the duct, with equal size along the axis, and of tetrahedral element in the outer domain.

Numerous tests were conducted to eliminate bias from numerical parameters [25]. In particular, the mesh size has been set to 6 elements by wavelength (for the minimum wavelength of the frequency range). A sphere radius of $R = 300$ mm was found to satisfy the radiation correction accurately for both the flanged and unbaffled configurations. Distances between the open end and the circular array for mode decomposition were adjusted, as well as the geometry and grid of the chamfer (un-baffled case) and of the finite flange. The final settings are listed in Table 2. An illustration of solution fields is provided in Figure 8 for the infinite flange configuration. In Figure 8a, the calculated pressure is a combination of different modes, all mixed in one complex field in the general case. Figures 8b, 8c and 8d show the calculated pressure at particular frequencies for which a single mode is dominant. It would be possible to excite essentially one single mode using a surface acceleration with a controlled spatio-temporal distribution, as shown in [25], but it has not been done here to remain close to the experimental situation.

The computed acoustic pressure is saved at virtual microphones placed at the same positions as in the experiments, that is, on the two rings of 8 microphones each, placed at position x_1 and x_2 (see Fig. 1). These estimates are post-processed as indicated in Section 2.3, using equations (11), (14) and (15).

4 Results

Results obtained from the numerical simulation presented in Section 3 and those obtained from the measurements presented in Section 2 are plotted in Figures 9 and 10, respectively for the modulus of the reflection coefficient given in equation (14) and the length correction given in equation (15). Evolutions from literature material or analytical derivation are also plotted, as listed in Table 3. All results are plotted as a function of the Helmholtz number ka, and also as a function of frequency. In the latter case, the frequency is obtained from the Helmholtz number according to $f = ka/(2\pi a/c_0)$ by taking for the speed of sound c_0 the experimental value, for all the curves.

For the unbaffled end, analytical results are taken from Rienstra [8] for higher modes and has been found identical to that reported by Snakowska et al. [32], and Levine and Schwinger [1] for the plane mode. It should be noted that

Table 2. Geometrical and numerical parameters of the simulations. See definitions in Figure 7. All lengths are in mm. The total guide length is $L = L^{'} + LB_i$ for $i = 1, 2, 3$ according to the termination.

a	$L^{'}$	s	LB_1	LB_2	LB_3	R	d	h	b	α
88	1210	40	120	280	110	300	53	15	30	20°

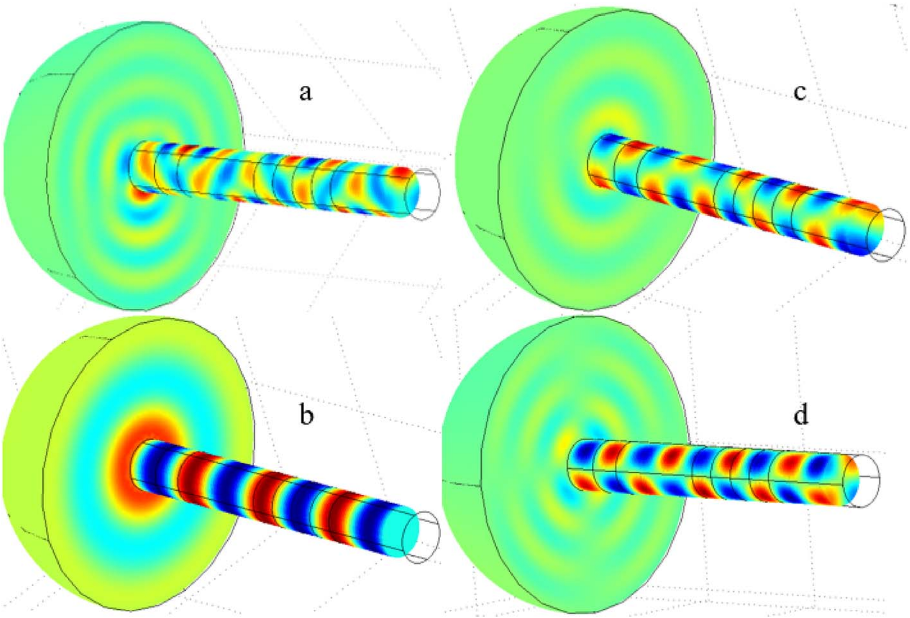

Figure 8. Total pressure field in the baffled pipe obtained with the numerical simulation, (a) combination of many modes at 2350 Hz, (b) plane mode is dominant at 1000 Hz, (c) mode (1, 0) is dominant at 1760 Hz and (d) mode (2, 0) is dominant at 2250 Hz.

these analytical models are for a duct which is semi infinite (that is, extends to $x = -\infty$ in the notations of Fig. 1). As argued in the end of Section 2.2, the fact that the inside of the duct, both in the experiments and in the numerical models, is ended by a rigid termination at $x = x_e$ is not in contradiction with this model, since the radiation impedance or reflection coefficient is independent of the left termination within the duct. However, outside the duct, the analytical model is slightly different from the experimental and numerical implementations. In the simulations, the way to approach the theoretically semi-infinite duct consists in using non-reflecting boundary conditions on the sphere limiting the domain outside the duct. In the experiments, the duct is necessarily truncated, so that the experimental geometry has some differences with both the numerical and theoretical geometries. However, as specified in Section 3, numerical convergence tests have indicated that the reflection coefficient is independent of the sphere radius when this radius is $R \geq 0.3$ m. This seems to indicate that the finite length of the duct in the experiments, which is about 1 m, is not critical for the reflection coefficient. In addition, it will be seen below that the agreement between the experiments and the analytical model tends to be better at low frequency than at high frequency. The finite extent of the duct being expected to have a larger effect at low frequency, this is further evidence that the finite length of the duct is not critical in this work.

Concerning the infinite flange, the evolution is obtained from analytical derivation using the theory of Zorumski [7]; this has been found identical to Norris and Cheng [4] for the plane mode. Finally, for the finite flange, the semi-empirical laws proposed by Dalmont et al. [5] are used. Note that no reference data could be found for this termination at higher modes. Comparison between the three estimation methods, and the behavior of higher-order modes, as well as the influence of termination, are discussed in the following sections.

4.1 Comparison between sources of data

Overall, measurements and simulations return similar decrease of the reflection coefficient and the length correction with the frequency. The termination influence emerges clearly from the spurious fluctuations for two first modes of both quantities. This provides cross validation of both estimation methods. By yielding smoother plots, the numerical results enable better reading of the evolution with frequency and comparison between terminations.

When available, the theoretical models reproduces the simulations with less than 5% error. Close to the onset frequencies, the agreement is better for the magnitude of the reflection coefficient, while it is worse for the length correction. The worst visible difference between numerical and theoretical values is noticed at the low-frequency limit

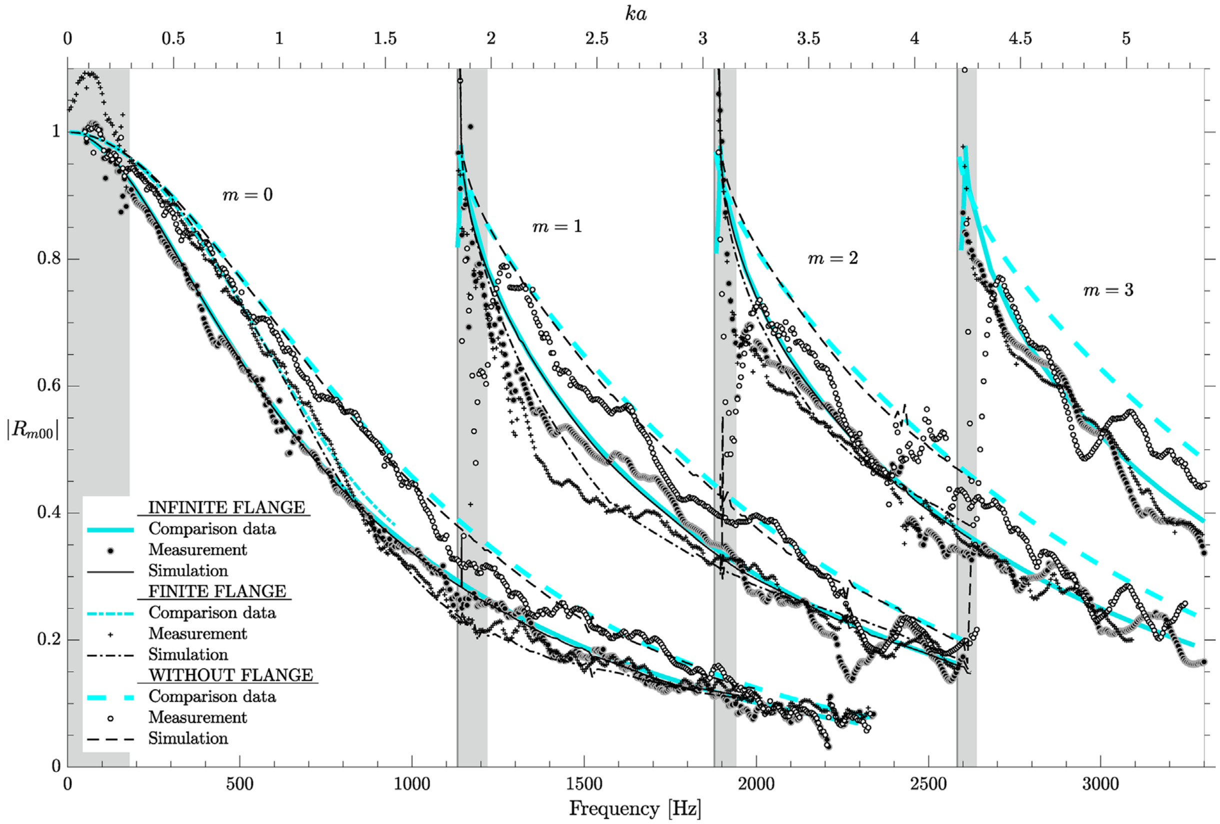

Figure 9. Modulus of the reflection coefficient for the tested ends and modes, plotted vs frequency. The corresponding Helmholtz number is indicated on the top axis. The grey band corresponds to uncertain frequency range for the corresponding mode onset, see Section 4.4. For comparison data details, see Table 3.

Table 3. Data used for comparisons in Figures 9 and 10. (*a*) stands for analytical derivation, (*m*) stands for measurements, (*n*) stands from numerical simulation.

Termination/mode (m, n)	(0, 0)	(1, 0)	(2, 0)	(3, 0)
Infinite flange	Present (*a*, according to Zorumski [7])			
Finite flange	Dalmont et al. [5] (*m*, *n*)			
Without flange	Levine and Schwinger [1] (*a*)	Rienstra [8] (*a*)		

for the finite flange, plane mode: Dalmont et al. returns $\delta/a \approx 0.73$ while the present simulations return $\delta/a \approx 0.70$.

4.2 Reflection coefficient and length correction for higher modes

For $m = 1$ and $m = 2$, the numerical results show non-horizontal onset, contrary to the plane mode, as predicted by theoretical formulas. Except this, the decrease of the reflection coefficient with frequency for higher modes follows the same tendency as that of the plane mode. The agreement between the measurements and the analytical derivation is noteworthy for $m = 3$, for which no simulation could be conducted due to computational costs.

As for the correction length, the experimental values asymptotically match the numerical and analytical ones with a slight negative offset, after a sharp increase from zero at the onset. The modes $m \geq 1$ exhibit an evolution that matches the plane mode, that goes grossly like $1/f$. Typically, one has $\delta/a \approx [0.4, 0.3, 0.22, 0.15]$ at $f \approx [1200, 1900, 2600, 3300]$ Hz, respectively. The dependency on m is weak as well as on the termination.

4.3 Influence of termination

For the plane mode, the magnitude of the reflection coefficient clearly differs for the different terminations and the three methods (experiments, theory, and simulations) agree on the same evolution: for low frequencies, the no flange and finite flange cases are very close to each other; as the frequency increases, the finite flange case gets closer to the infinite flange one. As a matter of fact, for wavelengths much smaller than the flange, the latter is seen as being infinite by the wave, whereas for wavelengths much larger than the flange the latter is assimilated as a non existing obstacle (no flange). This is clearly observed for the three sets of data, and was also observed in [5].

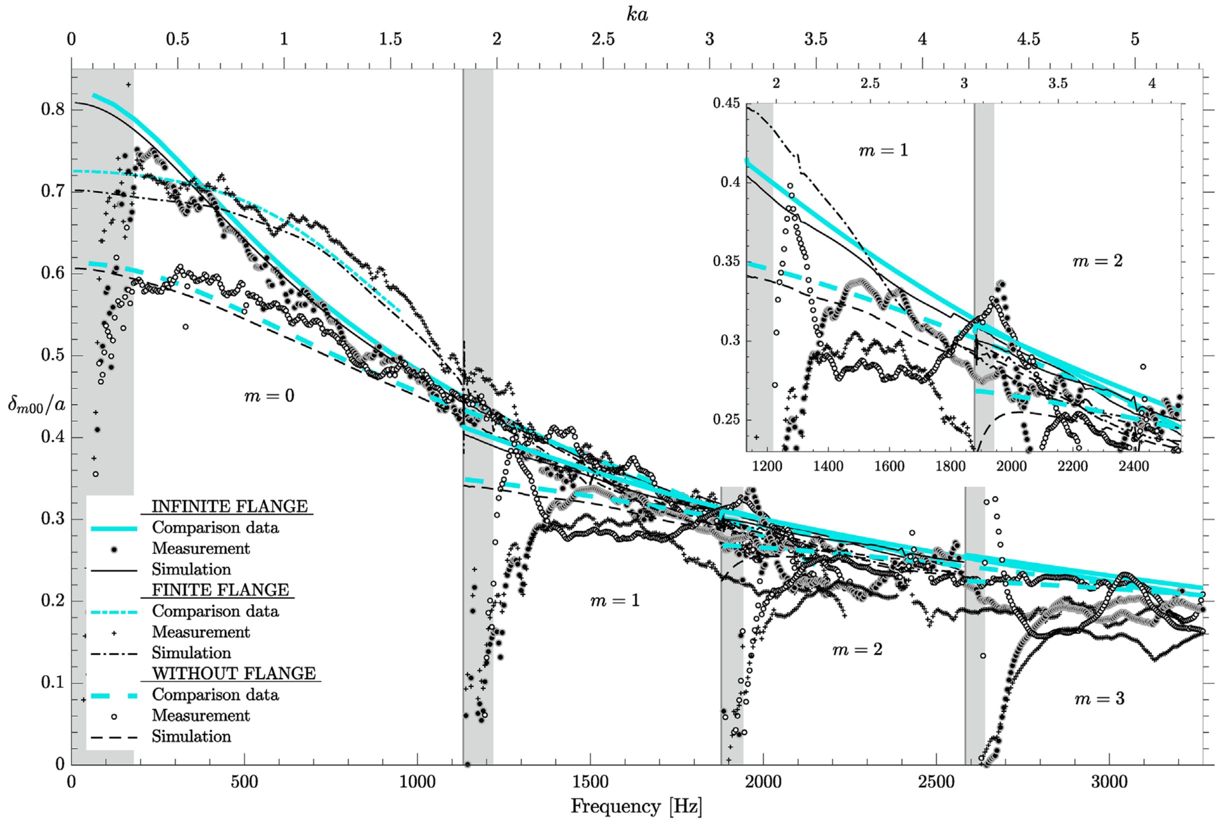

Figure 10. Length correction for the tested ends and modes, plotted vs frequency. The corresponding Helmholtz number is indicated on the top axis. The grey band corresponds to uncertain frequency range for the corresponding mode onset, see Section 4.4. For comparison data details, see Table 3.

However, for modes $m = 1$ and $m = 2$, the reflection coefficients computed from the simulations for the finite flange case are smaller in magnitude than for the infinite flange case for the lowest simulated frequencies; that is, the dash-dotted line is lower than the plain line. In particular, at 1600 Hz, one has $|R_{100}| \approx [0.40, 0.48, 0.58]$ with finite flange, infinite flange and without flange, respectively. Results of measurements for $m = 1$ and $m = 2$ above, and close to their respective cut-on frequencies show similar trends: infinite flange reflection coefficient (closed circles) has a higher magnitude than finite one (plus symbol), contrary to the plane mode case. For the highest mode ($m = 3$), the experimental results for the different terminations get very close to each others.

The influence of the termination on the end correction is about 10% at the mode cut-on, and then decreases with increasing frequency. In general, the finite flange end can not be considered as an intermediate condition between the unflanged and the infinite flange ends: this is only the case for the plane mode, at all frequencies for the reflection coefficient while only for $ka < 0.5$ for the end correction.

4.4 Error analysis

As was observed by previous authors (e.g. [21]), the greatest errors in the estimation of the reflection coefficient occur right above the cut-on frequency because the uncoupled model does not include evanescent contributions. In Figures 9 and 10, grey areas correspond to the frequency ranges for which the errors in the estimation of the modulus and phase of the reflection coefficient is a limiting factor. For higher modes, these ranges correspond to those proposed by [18, 20]; it is not the case for the plane mode. Indeed, the theoretical limits given by these authors for the two-microphone transfer function technique applied to the plane mode is $0.1\pi < ks < 0.8\pi$; this yields, for our experimental conditions a low frequency limit of 428 Hz. As apparent from Figures 9 and 10, the estimation of the reflection coefficient is satisfactory for frequencies lower than this limit. When considering (14), it is possible to estimate the origin and the value of the uncertainty in the reflection coefficient by listing and estimating the errors in the input data used to obtain this coefficient: temperature measurements, distance between microphones, distance from open end, pressure measurements. Setting uncertainties for these different quantities according to sensors and/or machining of pieces allows to analyse the origin of the final error [33]. It shows that the low-frequency error is mainly due to uncertainty in pressure measurements and set the limit frequency to 180 Hz. The low frequency limit actually observed in our measurement is lowered compared to Åbom and Bodén limit thanks to the use of the synchronous detection together with a sinusoidal excitation.

This extends the validity of the two-microphone method to lower frequencies.

5 Conclusion

The present paper studies acoustic wave reflection at different types of terminations, for the plane mode and the first three purely azimuthal higher modes, below Helmholtz numbers of 5.3. Experimentally, it was possible to distinguish the end-geometry effect on both the magnitude of the reflection coefficient and the end correction, although measurement noise increases with the mode order. Numerical calculation was developed to mimic the experiments and a satisfactory agreement was observed between calculated and measured reflection coefficients. Results were also compared to available previous studies so that multiple-cross-validation was proposed. The numerical simulation can be considered with confidence in order to extend the investigations to radial modes, not easily accessible by instrumentation, and to other forms of terminations. Moreover, the simulations give the external radiating field, useful in many applications, and could be extended to the situation in which a mean flow is present.

Acknowledgments

The authors thanks Abdelbasset HARRACHI for performing the numerical simulations during his Master thesis [25]. The comparison data for the higher modes at the unflanged end are based on [8] using a code written by Sandrine FAUQUEUX from ONERA, who is greatly acknowledged.

Conflict of interest

The authors declare that they have no conflicts of interest in relation to this article.

Data availability statement

Data are available on request from the authors.

References

1. H. Levine, J. Schwinger: On the radiation of sound from an unflanged circular pipe. Physical Review 73, 4 (1948) 383–406.
2. Y. Nomura, I. Yamamura, S. Inawashiro: On the acoustic radiation from a flanged circular pipe. Journal of the Physical Society of Japan 15 (1960) 510–517.
3. Y. Ando: On sound radiation from semi-infinite circular pipe of certain wall thickness. Acta Acustica United with Acustica 22, 4 (1969) 219–225.
4. A.N. Norris, I.C. Sheng: Acoustic radiation from a circular pipe with an infinite flange. Journal of Sound and Vibration 135, 1 (1989) 85–93.
5. J.-P. Dalmont, C.J. Nederveen, N. Joly: Radiation impedance of tubes ended with different flanges: Numerical and experimental investigation. Journal of Sound and Vibration 244, 3 (2001) 505–534.
6. M.C.A.M. Peters, A. Hirschberg, A.J. Reijnen, A.P.J. Wijnands: Damping and reflection coefficient measurements for an open pipe at low Mach and low Helmholtz numbers. Journal of Sound and Vibration 256 (1993) 499–534.
7. W.E. Zorumski: Generalized radiation impedances and reflection coefficients of circular and annular ducts. Journal of the Acoustical Society of America 54, 6 (1973) 167–1673.
8. S.W. Rienstra: Acoustic radiation from a semi-infinite annular duct in a uniform subsonic mean flow. Journal of Sound and Vibration 94, 2 (1984) 267–288.
9. A. Snakowska, J. Jurkiewicz: Efficiency of energy radiation from an unflanged cylindrical guide in case of multimode excitation. Acta Acustica United with Acustica 96 (2011) 416–424.
10. A. Snakowska, J. Jurkiewicz, D. Smolik: Open end correction for arbitrary mode propagating in a cylindrical acoustic waveguide. Acta Physica Polonica A 120 (2011) 736–739.
11. M.D. Dahl, R. Hixon, D.L. Sutliff: Further development of rotating rake mode measurement data analysis. AIAA Paper N^o 2013–2246, 2013.
12. M.D. Dahl, R. Hixon: Numerical predictions of mode reflections in an open circular duct: Comparison with theory. In: 21st AIAA/CEAS Aeroacoustics Conference 2015, 22–26 June 2015, Dallas, TX, 2015, p. 2524.
13. S. Félix, J.-P. Doc, M.A. Boucher: Modeling of the multimodal radiation from an open-ended waveguide. Journal of the Acoustical Society of America 143 (2018) 3520–3528.
14. R. Blandin, A. Van Hirtum, X. Pelorson, R. Laboissière: Multimodal radiation impedance of a waveguide with arbitrary cross-sectional shape terminated in an infinite baffle. Journal of the Acoustical Society of America 145 (2019) 2561–2564.
15. C.J. Moore: Measurement of radial and circumferential modes in annular and circular fan ducts. Journal of Sound and Vibration 62 (1979) 235–256.
16. P.D. Yardley: Measurements of noise and turbulence generated by rotating machines. PhD thesis. University of Southampton, 1975.
17. E.J. Kerschen, J.P. Johnston: A modal separation measurement technique for broadband noise propagating inside circular ducts. Journal of Sound and Vibration 76 (1981) 499–515.
18. M. Åbom: Modal decomposition in guides based on transfer function measurements between microphone pairs. Journal of Sound and Vibration 135, 1 (1989) 95–114.
19. J.Y. Chung, D.A. Blaser: Transfer function method of measuring in guide acoustic properties, I. Theory, II. Experiment. Journal of the Acoustical Society of America 68 (1980) 907–921.
20. M. Akoum, J.-M. Ville: Measurement of the reflection matrix of a discontinuity in a guide. Journal of the Acoustical Society of America 103, 5 (1998) 2463–2468.
21. J.L. Horner, Y. Hu: A hybrid modal decomposition approach for higher-order modes in circular ducts. Applied Acoustics 74 (2013) 122–133.
22. J.L. Horner, Y. Hu: Investigation into higher-order mode propagation through orifice plates in circular ducts. Applied Acoustics 74, 5 (2013) 728–739.
23. S. Fauqueux, R. Davy: Modal deconvolution method in a finite circular duct using flush-mounted microphones. In: 2018 AIAA/CEAS Aeroacoustics Conference, June 25–29, 2018, AIAA, Atlanta, Georgia, 2018, p. 3927.
24. A.F. Seybert, D.F. Ross: Experimental determination of acoustic properties using a two-microphone random-excitation technique. Journal of the Acoustical Society of America 61 (1977) 1362–1370.
25. H. Abdelbasset: Numerical simulation of multi-modal reflection in large acoustic waveguides with different terminations. MSc thesis. ENSTA ParisTech, 2018. https://hal.science/hal-04128810.

26. H. Bailliet, R. Boucheron, J.-P. Dalmont, Ph. Herzog, S. Moreau, J.-C. Valière: Setting up an experimental apparatus for the study of multimodal acoustic propagation with turbulent mean flow. Applied Acoustics 73 (2012) 191–197.
27. M. Bruneau: Fundamentals of acoustics. ISTE Publishing Company, 2005.
28. A. Selamet, Z.L. Ji: Wave reflections from guide terminations. Journal of the Acoustical Society of America 109, 4 (2001) 1304–1311.
29. W. Shao, C.K. Mechefske: Analyses of radiation impedances of finite cylindrical ducts. Journal of Sound and Vibration 286 (2005) 363–381.
30. C. Vanwynsberghe, R. Marchiano, F. Ollivier, P. Challande, H. Moingeon, J. Marchal: Design and implementation of a multi-octave-band audio camera for realtime diagnosis. Applied Acoustics 89 (2015) 281–287.
31. C.R. Lowis, P.F. Joseph, P. Sitjtsma: A technique for the in situ phase calibration of in-duct axial microphone arrays. Journal of Sound and Vibration 329, 22 (2010) 4634–4642.
32. A. Snakowska, J. Jurkiewicz, L. Gorazd: A hybrid method for determination of the acoustic impedance of an unflanged cylindrical duct for multimode wave. Journal of Sound and Vibration 396 (2017) 325–339.
33. Z. Qiu: Propagation en guide d'onde large: mesure par antennerie microphonique de la réflexion multimodale pour différentes extrémités. PhD thesis. Université de Poitiers, 2017.

Cite this article as: Marx D. Margnat F. Bailliet H. Prax C. Qiu Z, et al. 2024. Uncoupled multimodal wave reflection from guide termination with different flanges: Experimental and numerical investigation. Acta Acustica, **8**, 38.